

# Dataset for the synthesis and characterization of disordered metallic carbon materials from graphene edge chemistry

Katarzyna Z. Donato<sup>1</sup>, Gavin K. W. Koon<sup>1</sup>, Sarah J. Lee<sup>1</sup>, Alexandra Carvalho<sup>1,2</sup>, Hui Li Tan<sup>1</sup>, Mariana C. F. Costa<sup>1,2,3</sup>, Jakub Tolasz<sup>4</sup>, Petra Ecorchard<sup>4</sup>, Paweł P. Michałowski<sup>5</sup>, Ricardo K. Donato<sup>1\*</sup>, A. H. Castro Neto<sup>1,2,3\*</sup>

<sup>1</sup> Centre for Advanced 2D Materials, National University of Singapore, 117546, Singapore.

<sup>2</sup> Institute for Functional Intelligent Materials (I-FIM), National University of Singapore, 117544, Singapore.

<sup>3</sup> Department of Materials Science and Engineering, National University of Singapore, 117575, Singapore.

<sup>4</sup> Institute of Inorganic Chemistry of the Czech Academy of Sciences, Husinec-Řež 1001, 250 68 Řež, Czech Republic.

<sup>5</sup> Łukasiewicz Research Network, Institute of Microelectronics and Photonics, 02-668 Warsaw, Poland

E-mail: [donato@nus.edu.sg](mailto:donato@nus.edu.sg); [c2dhead@nus.edu.sg](mailto:c2dhead@nus.edu.sg)

## Table of Contents

<b>Abstract</b> .....	<b>2</b>
<b>Section S1. Simulations</b> .....	<b>3</b>
S1.1 Density-functional theory (DFT) calculations of graphene hydrolysis .....	3
S1.2 Molecular dynamics simulation of interactions among edge-hydrolyzed species .....	5
<b>Section S2. Materials and synthetic methods</b> .....	<b>7</b>
S2.1 Graphene sources .....	7
S2.2 Graphene edge-hydrolysis protocol.....	8
S2.3 Graphene edge-hydrolysis characterization .....	10
S2.4 Preparation of self-assembled films .....	13
S2.5 Preparation of films on complex surfaces and confined spaces.....	14
S2.6 Mild annealing and film crosslinking.....	15
<b>Section S3. Stability and processability</b> .....	<b>16</b>
<b>Section S4. Mechanical properties</b> .....	<b>17</b>
<b>Section S5. Thermal transport</b> .....	<b>19</b>
<b>Section S6. Electrical transport</b> .....	<b>21</b>
<b>Section S7. Compositional, morphological and physicochemical characterization methods</b> .....	<b>23</b>
<b>Section S8. G<sup>0r</sup>'s properties summary</b> .....	<b>26</b>
<b>Acknowledgement and funding information</b> .....	<b>26</b>
<b>References</b> .....	<b>27</b>

## ***Abstract***

This dataset provides a comprehensive account of the intricate processes involved in the rational design, synthesis, and characterization of anisotropic metallic carbon materials. The materials were derived through the hydrolytic oxidation of graphene sheets, followed by meticulous self-assembly and mild annealing. The resulting products are highly percolated carbon networks, preserving the essential basal area of the source graphene.

Structured into various sections, this dataset aims to furnish detailed insights crucial for supporting extensive investigations into these carbon materials. Section S1 delves into simulations that elucidate the reactivity of hydroxyl radicals in the hydrolytic oxidation process, pinpointing optimal conditions for their selective use in edge-hydrolysis of graphene. Additionally, it explores the molecular dynamics of edge-hydrolyzed graphene sheets, unraveling their self-assembly behavior and the formation of highly ordered films.

Section S2 meticulously describes the source materials and optimal protocols, aligning with insights gained from simulations. In Section S3, the dataset explores the impact of synthesis protocols on the processability of hydrolyzed graphene and anticipates potential applications. Sections S4 to S7 present detailed characterization protocols, meticulously divided into morphology, composition, mechanical properties, and thermal/electronic transport, ensuring the inclusion of all essential details for reproducibility in core characterizations. Finally, Section S8 presents a table summarizing the general properties of the final annealed metallic carbon film ( $G^0$ ).

This dataset thus serves as a valuable resource, providing a robust foundation for in-depth studies and fostering a comprehensive understanding of the multifaceted aspects of anisotropic metallic carbon materials.

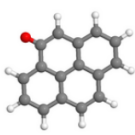
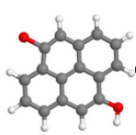
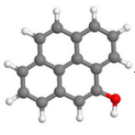
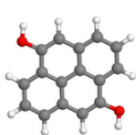
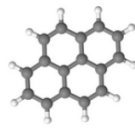
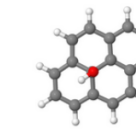
## **Section S1. Simulations**

### *S1.1 Density-functional theory (DFT) calculations of graphene hydrolysis*

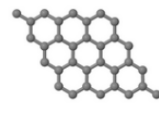
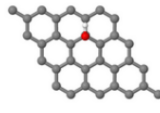
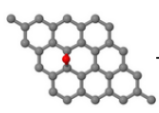
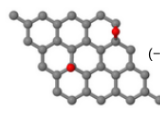
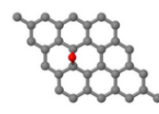
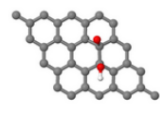
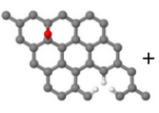
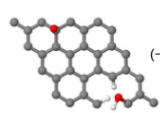
First-principles calculations were based on the framework of DFT, as implemented in Quantum ESPRESSO<sup>[1]</sup>, with the PBE<sup>[2]</sup> exchange and correlation functional. Ultra-soft pseudo-potentials of the RRKJUS type were used<sup>[3]</sup>. We employed a plane wave basis set with kinetic energy cutoffs of 40 Ry for the wave functions. The Van der Waals interactions were described using the potential of Grimme<sup>[4,5]</sup>. Both supercell and nanoflake models were used. The flakes had 16 carbon atoms per layer, whereas the supercell model contained 32 atoms per layer. For the latter, the Brillouin zone was sampled using a  $\Gamma$ -centered  $6\times 6\times 1$  Monkhorst-Pack (MP) grid<sup>[6]</sup>. A supercell periodicity of 30-40 Angstrom in the direction perpendicular to the layers was used to avoid spurious interactions between replicas.

We have calculated the reactions enthalpies ( $\Delta H_r$ ) of hydroxyl with different functional groups at the edges of graphene, at its basal plane, or at defect sites, which corresponds to the difference between the total energies of reagents and products (Tables S1 and S2). A negative value indicates energy release. To respect charge balance, some reactions require the transfer of an electron either to the graphene or to a defect. Thus, we have modelled some of the reactions in the presence of either an epoxy or a hydroxyl radical, both of which can become negatively charged. When negatively charged, the epoxy relaxes to a carboxyl configuration.

**Table S1.** Reactions on finite graphene flakes (*F*) and respective reaction enthalpies, calculated using DFT calculations.

#	Reagents	Products	Reaction	$\Delta H$ (eV)
A	 + 2 OH <sup>-</sup>	 <sup>(-2)</sup> + H <sub>2</sub> O	$F\text{-H} + 2 \text{OH}^- \rightarrow F\text{-OH}^{(-2)} + \text{H}_2\text{O}$ (in the presence of a ketone group)	-4.20
B	 + 2 OH <sup>-</sup>	 <sup>(-2)</sup> + H <sub>2</sub> O	$F\text{-H} + 2 \text{OH}^- \rightarrow F\text{-OH}^{(-2)} + \text{H}_2\text{O}$ (in the presence of a hydroxyl group)	-2.87
C	 + OH <sup>-</sup>	 <sup>(-)</sup>	$F + \text{OH}^- \rightarrow F\text{-OH}^-$	-0.91

**Table S2.** Reaction energies on infinite graphene sheets (*G*), with or without defects.

	Reagents	Products	Reaction	$\Delta H$ (eV)
D	 + OH <sup>-</sup>	 <sup>(-)</sup>	$G + \text{OH}^- \rightarrow G\text{-OH}^-$	0.07
E	 + 2 OH <sup>-</sup>	 <sup>(-2)</sup> + H <sub>2</sub> O	$G + 2 \text{OH}^- \rightarrow G\text{-O}^{(-2)} + \text{H}_2\text{O}$ (in the presence of epoxy/carboxyl)	-1.06
F	 + OH <sup>-</sup>	 <sup>(-)</sup>	$G\text{-O} + \text{OH}^- \rightarrow G\text{-O-OH}^-$	0.51
G	 + 2 OH <sup>-</sup>	 <sup>(-2)</sup> + H <sub>2</sub> O	$G:\text{VH}_3 + 2 \text{OH}^- \rightarrow G:\text{VOH}_3^{(-2)} + \text{H}_2\text{O}$ (in the presence of epoxy/carboxyl group)	-3.16

### *S1.2 Molecular dynamics simulation of interactions among edge-hydrolyzed species*

Molecular dynamics simulations were performed using the LAMMPS code<sup>[7]</sup>. The inter-atomic interactions were modelled using the classical reactive force field potential of Chenoweth *et al.*<sup>[8]</sup>. The graphene flakes were semi-infinite ribbons with serrated edges, composed of 9234 atoms, which were initially created using Jmol<sup>[9]</sup>. The interaction between flakes was achieved by imposing periodic boundary conditions, such that the nanoribbon repeats itself along the directions perpendicular to the edges, thus allowing for edge-edge interactions. Additionally, we performed similar calculations for a four-layer graphene flake in vacuum, for comparison between thin sheet clusters and infinitely thick ones.

Periodic boundary conditions were applied along the direction perpendicular to the edges, allowing parallel edges of neighboring nanoribbon images to interact in-plane (Figure S1). Additionally, we have also constructed a 3D model where the repetition along the direction perpendicular to the basal plane allowed the edges to interact both with the adjacent graphene ribbon images above and below (Figure S1-c). After initial optimization and thermalization, the annealing of the flakes was simulated within the isothermal-isobaric ensemble for 0.4 ns at 300 K, 400, 500, and 600 K, at a pressure of 0 atm, using a Nosé-Hoover thermostat style integration, with an integration timestep of 0.1 fs. The y-direction cell dimension was kept fixed during the calculations, while the periodic x (or x and z) direction(s) were allowed to relax in the 2D (3D) models.

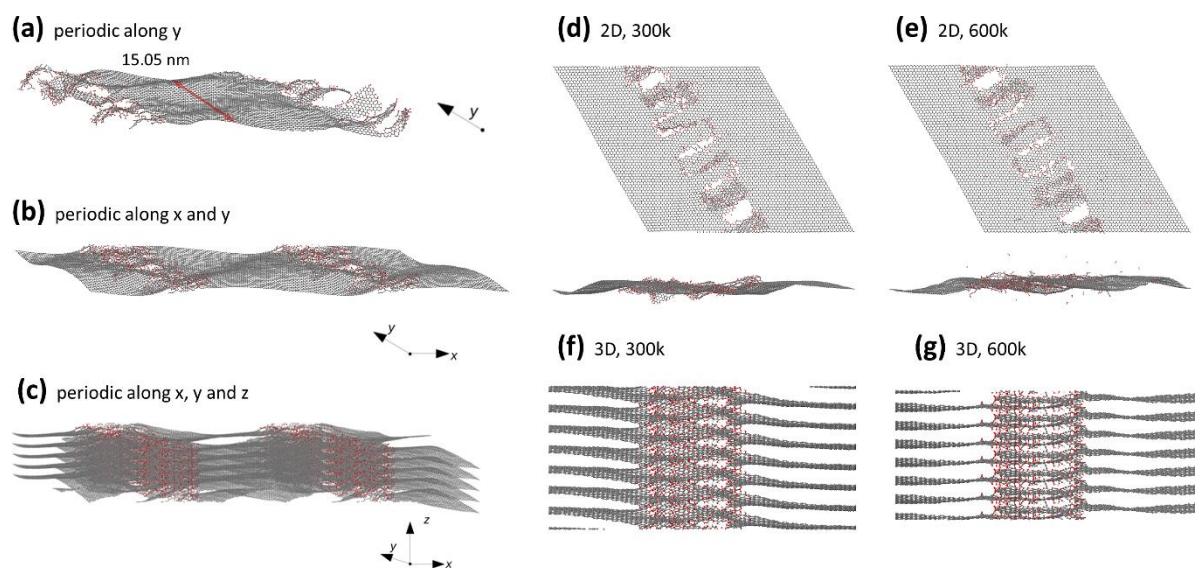


**Figure S1.** Scheme of the periodic model used to simulate in-plane and out-of-plane edge interactions between  $G_{eh}$  layers. (a) isolated flake; (b) 2D model and (c) 3D model. Molecular dynamics simulations of interacting  $G_{eh}$  species in function of the temperature: (d-e) 2D model at 300 K and 600 K, top and side views; (f-g) 3D model at 300 K and 600 K, side view (a slice is shown for clarity).

## Section S2. Materials and synthetic methods

### S2.1 Graphene sources

To prospect the generality of the process, three commercial sources of graphene nanoplatelets (GNP) were functionalized using the  $G_{eh}$  platform. As we do not believe it's relevant for the process, we do not reveal their names, but their structural properties, carbon material quality-related properties, and elemental analysis are summarized in Tables S3 and S4. We must highlight that the three graphene sources used below were tested and two of them yielded good quality products (GNP 1 and GNP 3), while GNP 2 led to less reliable and lower quality products (dramatic decrease in selectivity). The results presenting the different levels of oxidation were focused on GNP 3 for practicality.

**Table S3.** Relevant carbon-related characteristics of graphene sources used for functionalization with  $G_{eh}$ .

Sample	Flake size ( $\mu\text{m}$ )		Number of layers		Flake quality		Carbon composition (%)				
	DF <sub>50</sub>	DF <sub>90</sub>	DL <sub>50</sub>	DL <sub>90</sub>	$I_G/I_{2D}$	$I_D/I_G$	C sp	C sp <sup>2</sup>	C sp <sup>3</sup>	C-O	C=O
GNP 1	>0.5	>1.1	<10	<50	~1.9	~0.4	3.32	55.43	16.03	18.88	6.34
GNP 2	>0.5	>1.1	<30	<300	~2.50	~0.3	0	66.10	20.02	6.07	7.80
GNP 3	>0.8	>1.8	<10	<30	~2.83	~0.2	0	78.69	12.16	6.00	6.34

*DF<sub>50</sub> and DL<sub>50</sub> are the median values for flake lateral size obtained via optical microscopy and the number of layers obtained via AFM, respectively. DF<sub>90</sub> and DL<sub>90</sub> are obtained in the same manner, but their values represent where lies 90% of the distribution.  $I_G/I_{2D}$  and  $I_D/I_G$  are obtained via Raman spectrometry. The carbon composition and oxidation are obtained by XPS.*

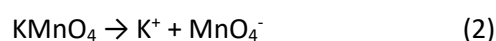
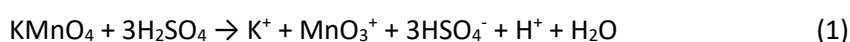
**Table S4.** Elemental analysis of graphene sources used for functionalization with  $G_{eh}$ .

Sample	Elemental analysis (%)					
	C	H	N	S	O	Total
GNP 1	78.1	2.1	0	0.1	16.6	96.9
GNP 2	95.7	0.3	0.1	0.1	1.0	97.2
GNP 3	96.6	0.2	0	0.2	3.0	100

## S2.2 Graphene edge-hydrolysis protocol

Our platform allows for highly concentrated selective edge hydrolysis reactions (up to 5.7%) and, consequently, very high product outputs. Using a 1L reactor as a reference, batches with up to 57 grams can be processed in cycles as short as 2 hours, resulting in reaction rates up to ~28 g/Lh (prior to dilution, details below).

The basic initiation of the oxidation reaction based on sulfuric acid and potassium permanganate is the same as in the classic Hummer's method (Eq. 1-3).



However, the presence of water and Mn(VII) (3:1 molar ratio) leads to the formation of  $\text{O}_3$ , which degrades into  $\cdot\text{O}$  and especially  $\text{HO}\cdot$  (by the further reacting of  $\text{O}_3$  with  $\text{H}_2\text{O}$ )<sup>[10]</sup>. These radicals are highly reactive and, when in the presence of graphene, will react promptly forming a hydroxyl-group-rich structure. For this reason, temperature control is essential to avoid random reactions and for promoting selective functionalization. In sum, many functionalization variations can be applied to graphene using simple modifications of the classic chemical oxidation processes, enabling scaling-up the production of interesting new applications of modified graphene such as 2D electrolytes<sup>[11–15]</sup>.

Thus, concentrated sulfuric acid ( $\text{H}_2\text{SO}_4$ , 95-98%) is initially added to a reactor and cooled down to 5°C under constant stirring. Then, graphene/micronized graphite is added to the  $\text{H}_2\text{SO}_4$ , where the ratio graphene/acid defines the final level of oxidation/functionalization (Figure S2, step 1). The maximum concentration supported by this process (due to viscosity restrictions), yielding the mildest oxidation, is 210 mg of graphene per 1 mL of  $\text{H}_2\text{SO}_4$ . After stirring until complete graphene dispersion, forming a black viscous liquid (about 5-10 min), a pre-cooled 5%  $\text{KMnO}_4$  aqueous solution is slowly added using a peristaltic pump, keeping the temperature constant between 5 and 10°C



(Figure S2, step 2). This process takes up to 1 h, depending on the reaction volume and flow applied, where the total amount of  $\text{KMnO}_4$  is set to 133 mg per 1 mL of  $\text{H}_2\text{SO}_4$ . At this stage the formation of  $\cdot\text{OH}$  and  $\cdot\text{O}$  radicals takes place, but the reactivity of the radicals is kept lower due to the low temperature. After  $\text{KMnO}_4$  addition, the temperature is increased to  $22^\circ\text{C}$  for 20 min (oxidation/functionalization stage) (Figure S2, step 3). Since the level of oxidation can be adjusted for fine-tuning of properties, Table S5 summarizes the ratios of reactants to obtain the three different C/O ratios as described in Table S6 ( $G_{\text{eh}(6)}$ ,  $G_{\text{eh}(10)}$  and  $G_{\text{eh}(15)}$ ).

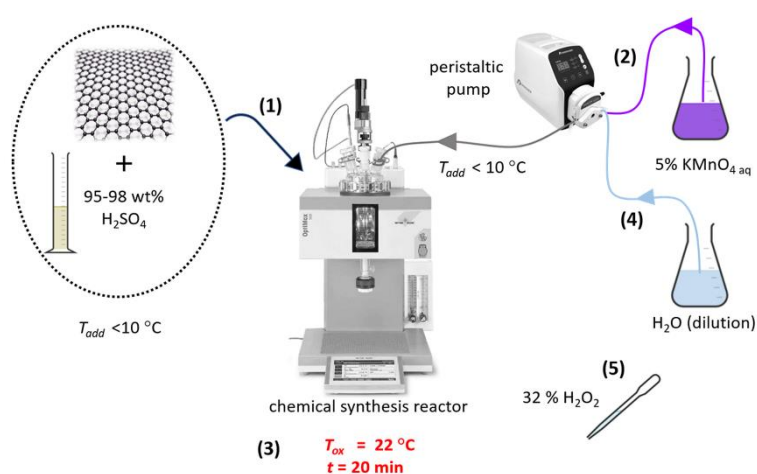


**Figure S2.** Schematic representation of the selective edge-hydrolysis reaction setup ( $G_{\text{eh}}$ ), including the reaction steps: (1) graphene and sulfuric acid addition; (2) potassium permanganate solution addition; (3) temperature increase to  $22^\circ\text{C}$  for  $\sim 20$  min (oxidation/ functionalization step); (4) dilution with water; (5) reaction quenching.

Since the temperature is kept low during the radical formation period, the decreased intercalation associated with the overall decreased radical reactivity (but with increased reactivity at the graphene's edges in relation to the basal plane) will greatly favor the functionalization at the graphene's edges. After the reaction, the resulting suspension is cooled to  $5^\circ\text{C}$ , diluted (2 mL of  $\text{H}_2\text{O}$  per 1 mL of  $\text{H}_2\text{SO}_4$ ) (Figure S2a, step 4), quenched with a 35%  $\text{H}_2\text{O}_2$  solution (0.06 mL  $\text{H}_2\text{O}_2$  per 1 mL 5%  $\text{KMnO}_4$ ) (Fig. S2a, step 5), and left stirring for 2 h at RT. Then, the resulting suspension is transferred to a separation funnel and left overnight to precipitate. The precipitated slurry is then separated and cleaned with 1 cycle of washing using 10% HCl (7 mL of HCl per 1 mL  $\text{H}_2\text{SO}_4$ ). For

applications demanding higher purity, the washed slurry is dialyzed (10 kDa molecular weight membrane) until stable pH.

**Table S5.** Reactant ratios for obtaining the systems with different levels of oxidation.

Sample	Graphene (g)	H <sub>2</sub> SO <sub>4</sub> (mL)	KMnO <sub>4</sub> (g)	H <sub>2</sub> O (mL)
G <sub>eh(6)</sub>	1.00	13.60	1.80	34.20
G <sub>eh(10)</sub>	1.00	6.80	0.90	17.10
G <sub>eh(15)</sub>	1.00	4.80	0.64	12.16

### S2.3 Graphene edge-hydrolysis characterization

The proposed reaction mechanism is demonstrated by preparing G<sub>eh</sub>, following the protocol in Section S2.2, the products characterizations are presented in Figures S3 and S4. For brevity, the samples with varying oxidation are assigned based on the C/O ratio, e.g. a G<sub>eh</sub> with C/O = 6 is assigned as G<sub>eh(6)</sub> before annealing, and G<sub>eh(6a)</sub> after annealing.

Very high carbon contents (up to 89% C), mainly represented by C sp<sup>2</sup> are observed for all samples, even with increasing oxidation (Figure S3a). When the most oxidized sample (G<sub>eh(6)</sub>) is annealed at 150°C, the number of functional groups decreases to less than half, with a mild increase in C sp<sup>3</sup> (Figure S3a) associated to the condensation reactions among sheets (see Section S2.5). The graphitic basal plane preservation also gives rise to high thermal stability (Figure S3b), with temperatures of maximum degradation ( $T_{\max}$ ) above 600°C (under oxidative atmosphere) for all oxidation levels, which are higher than those expected for GO<sup>[16]</sup>. The lack of functional groups in the basal plane also leads to the absence (for G<sub>eh(10)</sub> and G<sub>eh(15)</sub>) or presence of a broad XRD (001) diffraction peak (for G<sub>eh(6)</sub>), which is also shifted to a higher  $2\theta$  (*i.e.* smaller interlayer distance). The (002) diffraction peak is also slightly shifted to lower  $2\theta$ , with decreased intensity and broader profile as oxidation increases. This indicates that the re-stacked layers increasingly curve with enlarging the oxidized edge area (Figure S3c)<sup>[17]</sup>, which is also more prone to defect-dependent corrugation<sup>[18]</sup>. All systems form stable dispersions in water, but present dominant  $\pi$ - $\pi^*$  transitions of C sp<sup>2</sup>, observed by the UV/Vis absorbance band at  $\lambda_{\max} = 269$  nm (Figure S3d).

The Raman profiles are similar among the different systems with varying levels of functionalization (Figure S3e). However, different sheet regions within the same sample present a defined variation in Raman profile, with increased defects contiguous with the edges. The Raman maps in Figure S3f demonstrate this phenomenon in more detail, by comparing the distribution of intensities of graphene's fingerprint bands related to the primary mode representing the planar configuration  $sp^2$  bonded carbon (G band), the defect band representing a ring breathing mode from  $sp^2$  carbon rings (D band) and the second order of the D-band (2D band). By observing the difference in the distribution of color intensities of the D, G, and 2D maps, the reduced defects at the basal plane can be clearly evidenced.

Raman profiles also give us the defects distribution of the samples, revealing the defined hydrolysis imposed by the water-enhanced oxidation (see Section S2.2). However, SEM/EDX elemental mapping of C and O throughout the system clearly shows that these edge defects are associated to a defined oxidative hydrolysis process (Figure S4a). The maps obtained from  $G_{eh}$  show a very defined C elemental distribution coinciding with the  $G_{eh}$  aggregates. Moreover, the O elemental maps show very defined O concentration at the edges and rarefaction at the center of the flakes as a result of the mild and selective oxidation of this process. These results corroborate with the basal plane (Figure S4b) and edge (Figure S4c) localized elemental distribution obtained by HRTEM/EDX, and with the Raman maps for this system (Figure S3f).

**Table S6.** Elemental and functional composition of  $G_{eh}$  with different C/O ratios ( $G_{eh(x)}$ ), also showing values for graphene and GO for differentiation.

	C% <sup>4</sup>	H% <sup>4</sup>	N% <sup>4</sup>	S% <sup>4</sup>	O% <sup>4</sup>	Total% <sup>4</sup>	C/O ratio <sup>4</sup>	-COH <sup>5</sup>
<b>GO</b> <sup>1</sup>	39.1	4.4	0	2.3	52.2	98.0	0.8	-
<b><math>G_{eh(6)}</math></b> <sup>2</sup>	78.8	0.9	0	1.3	12.3	93.2	6.4	28.8±1.6
<b><math>G_{eh(10)}</math></b> <sup>2</sup>	87.3	0.7	0	1.1	8.6	98.1	10.2	20.7±1.4
<b><math>G_{eh(15)}</math></b> <sup>2</sup>	89.4	0.4	0	0.6	5.8	96.3	15.4	16.7±2.9
<b>Graphene</b> <sup>3</sup>	96.6	0.2	0	0.2	3.0	100.0	32.2	-

<sup>1</sup> Characterized from a commercial GO; <sup>2</sup> The value added to X in  $G_{eh(x)}$  refers to the C/O ratio; <sup>3</sup> GNP 3 was used as reference (details in Section 2.1). <sup>4</sup> Obtained by elemental analysis. <sup>5</sup> Obtained by XPS (Figure S3a).

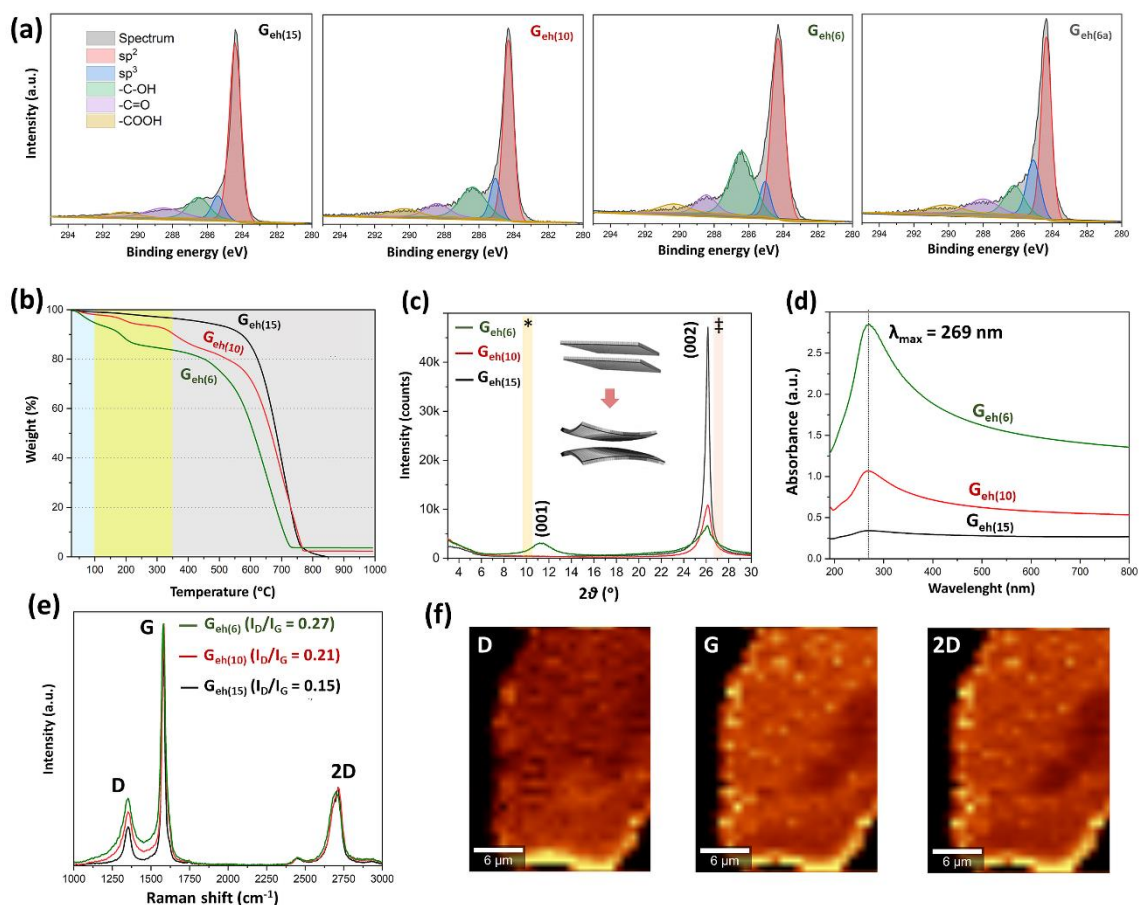


**Figure S3.** (a) High-resolution XPS demonstrating a dominant C 1s peak and a majority of C-O segments among the oxidation species, which increase with oxidation level ( $G_{eh(15-6)}$ ). The most oxidized sample ( $G_{eh(6)}$ ) was also submitted to annealing at 150°C ( $G_{eh(6a)}$ ), showing -COH values decreasing to half. (b) TGA highlighting the increase in mass loss at low temperatures with increasing oxidation. (c) XRD highlighting the expected  $2\theta$  angles for GO interlayer spacing (\*) and the 002 plane of graphite (‡), demonstrating the absent/shifted peaks for all oxidation levels and increased sheet curvature with oxidation. (d) UV-Vis of water dispersions of  $G_{eh(6-15)}$  with a dominant band at 269 nm. (e) Averaged Raman spectra of  $G_{eh(15-6)}$  showing relatively mild changes with varying the oxidation. (f) Raman mappings of an isolated large  $G_{eh(6)}$  flake showing the distributions of the intensity of the D, G and 2D bands.

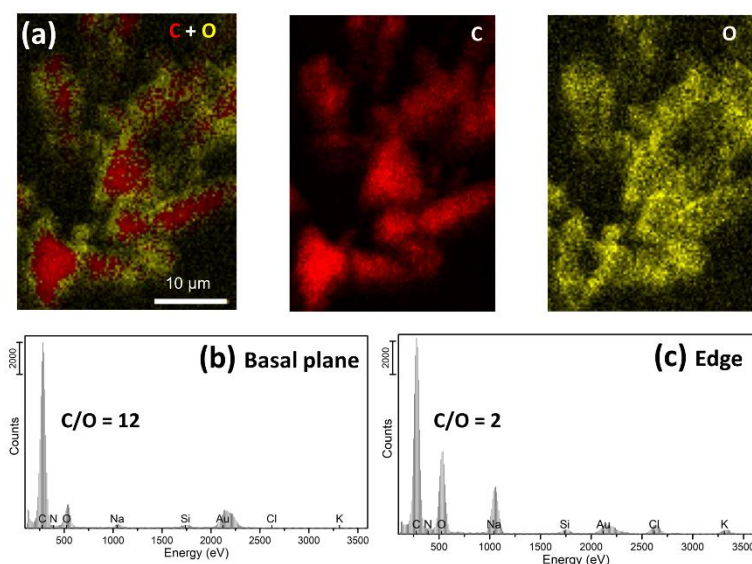


**Figure S4.** (a) SEM/EDX elemental maps of carbon (C) and oxygen (O) and (b) HRTEM/EDX localized elemental analysis of  $G_{eh(6)}$ , highlighting the large discrepancy between the C/O ratios at the basal plane (C/O = 12) and (c) edges (C/O = 2).

#### S2.4 Preparation of self-assembled films

After functionalization, the  $G^0$  films were prepared by redispersion of  $G_{eh}$  in a water:isopropanol mixture (1:1 volume ratio) and submitted to bath ultrasound (300 W) for 30min. The resulting dispersion was centrifuged at 3000 RPM for 15min, followed by another centrifugation at 6000 RPM for 15min, to remove any aggregates that could disturb the film formation. The resulting supernatant is a very homogenous shiny black dispersion presenting a liquid crystal-like appearance. At this stage, the organization of the dispersion seems to be strongly assisted by the interaction between the functionalized regions of  $G_{eh}$  and the solvents applied. Although  $G_{eh}$  is stable also in pure water, we have noticed that water:isopropanol mixtures produce more ordered and stable dispersions. Then, the supernatant was applied for film formation via direct solvent casting on a Teflon mold and via vacuum filtration using a PTFE filtration membrane (0.2-1  $\mu\text{m}$  pore sizes, depending on the lateral size of the source graphene used).

The highly ordered films can be formed using dispersions with a broad concentration range, from as low as 0.01 mg/mL to as high as 20 mg/mL. However, the ideal concentration for the film

formations, *i.e.* highest concentration with impeccable structural order and surface smoothness, is  $\sim 5$  mg/mL. This also reinforces the idea that the high structural order of the final films is implied by the material's anisotropy and interaction (both amongst sheets and solvent), suggesting lower initial entropy and consequently lower energy demand to form the highly ordered films.

### *S2.5 Preparation of films on complex surfaces and confined spaces*

Film formation on non-flat surfaces, surfaces bearing specific textures, or areas under confinement is highly demanded in areas dealing with the challenges of miniaturization, such as electronics<sup>[19]</sup>, where heat management in confined areas is a major issue<sup>[20]</sup>. Thus,  $G_{\text{eh}(6)}$  was cast onto a  $\text{SiO}_2$ -coated Si surface with a 50x50 micropillars array (100  $\mu\text{m}$  diameter and 100  $\mu\text{m}$  height pillars within a 100  $\text{mm}^2$  area). For that, 250  $\mu\text{L}$  of a 4mg/mL  $G_{\text{eh}(6)}$  dispersion in water/isopropanol (1:1 ratio) were casted onto the texturized substrate, forming a stable droplet. The droplet was left to evaporate (about 30min) within a fume hood with constant air flow, producing a 1mg film ( $\sim 10$   $\mu\text{m}$  thickness). Without any further treatment, the substrate was submitted to Raman, AFM and SEM characterizations.

The main goal here is to approximately simulate a thermal sink region for a chip stack on a "system on Package" (SoP) electronics package<sup>[21]</sup> and prepare *in-situ* a  $G^0$  thermally conductive film to dissipate the heat produced by the tightly packed transistors in SoP (details in the Experimental Methods).

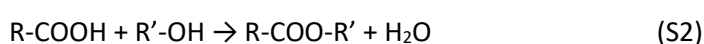
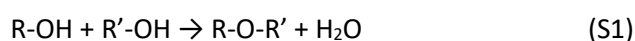
A high-quality  $G^0$  film is formed on the array, showing a smooth surface (Figure 4b) and defined fingerprint Raman bands of graphitic materials (Figure 4c). The same coated array was also submitted to a new deposition layer of  $\text{SiO}_2$ , confining the film within a dielectric/conductive/dielectric layered conformation. This conformation closely resembles the one in SoP, in order to guarantee thermal conductivity while electrically insulating the thermal sinking layer from the surroundings. The SEM/EDX image with overlaid and segregated C, O and Si elemental maps reveals the elemental compositions of the different sections of the partially deposited array, as

a function of the elemental composition at the uppermost layer. The elemental maps reveal the C-rich surface at the right section ( $G^0/SiO_2$ ) and the Si and O richer surface of the left section ( $SiO_2/G^0/SiO_2$ ), proving effective the association between film casting and deposition methods to form fully integrated complex layered structures.

### *S2.6 Mild annealing and film crosslinking*

The films were annealed at  $\sim 150^\circ\text{C}$ , and their structure was dramatically affected. The exothermic transformation at  $197^\circ\text{C}$  (up to  $111\text{ J/g}$  for  $G^0_{(6)}$ , by DSC), which is associated to a defined mass loss at the same temperature (up to 3wt% loss for  $G^0_{(6)}$ , by TGA), is the result of condensation reactions among the functional groups. Most of the functionalities are hydroxyl groups (see Figure S3a), but also some carboxyl groups can be added during synthesis or heating<sup>[22]</sup>, which can react forming ether, ester and anhydride bridges among the sheets. The mass loss observed by TGA can be directly associated to the evaporation of the water, and less frequently other molecules such as ethyl alcohol, produced by the different possible mechanisms of these reactions<sup>[23]</sup>. These reactions allow further structuration and the crosslinking of the films, allowing their reinforcement at a much milder temperature than graphitization processes and avoiding temperature-related limitations to their applications. After crosslinking the  $G_{\text{eh}}$  species are very thermal resistant even in oxidative atmospheres, with thermooxidative decomposition temperatures above  $600^\circ\text{C}$  (Figure S5b).

Examples of the possible condensation reactions happening during the crosslinking are summarized in Equations S1-S4. This takes into consideration the functional groups available at  $G_{\text{eh}}$  edges and the most common condensation reaction mechanisms (Eq. S1-S3), including Claisen and Dieckmann condensations (S4).



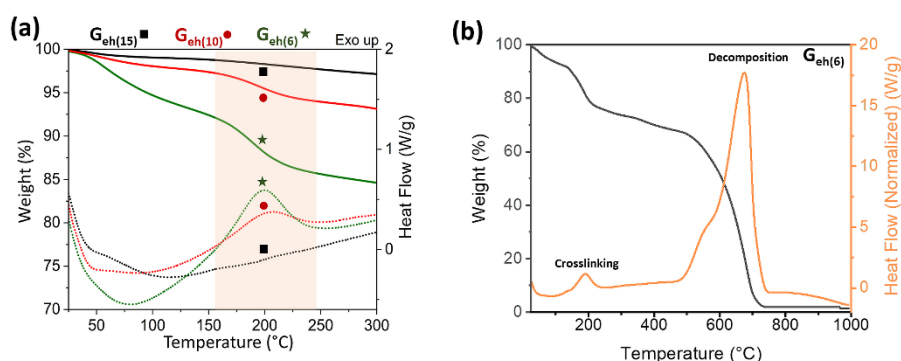


**Figure S5.** (a) detailed TGA/DSC analysis of the  $G_{eh}$  species with different oxidations, highlighting the exothermic transformation with onset at  $\sim 150^{\circ}\text{C}$ . (b) TGA/DSC analysis of the  $G_{eh(6)}$  showing a high thermooxidative decomposition temperature ( $T_{\text{onset}} \sim 600^{\circ}\text{C}$ ).

### Section S3. Stability and processability

After the functionalization reactions, different products can be easily obtained, such as water-stable dispersion, highly concentrated and dispersible slurry, extruded or compressed films, pastilles and filaments, free-standing films, and films deposited in complex texturized surfaces, etc. (Figure S6a). The high stability in water and solvent mixtures allows for the preparation of film even from very concentrated dispersions (up to 4%). Also, the strong anisotropy and sheet assembly, associated to a lower solvent content, allows for the fast preparation of large films without disrupting the film structure. Importantly, the annealing/crosslinking is performed without the application of vacuum or inert atmosphere, as  $G_{eh}$ 's thermal decomposition temperature ( $T_d$ ) is much higher than the annealing temperature (see Figure S5b), and the presence of small amounts of water facilitates an effective crosslinking by causing an anti-plasticization of the films<sup>[24]</sup>. Consequently, large films can be prepared both at room temperature or by hot processing (casting or pressing), and the film size can be indefinitely expanded, limited only by the casting/pressing support.



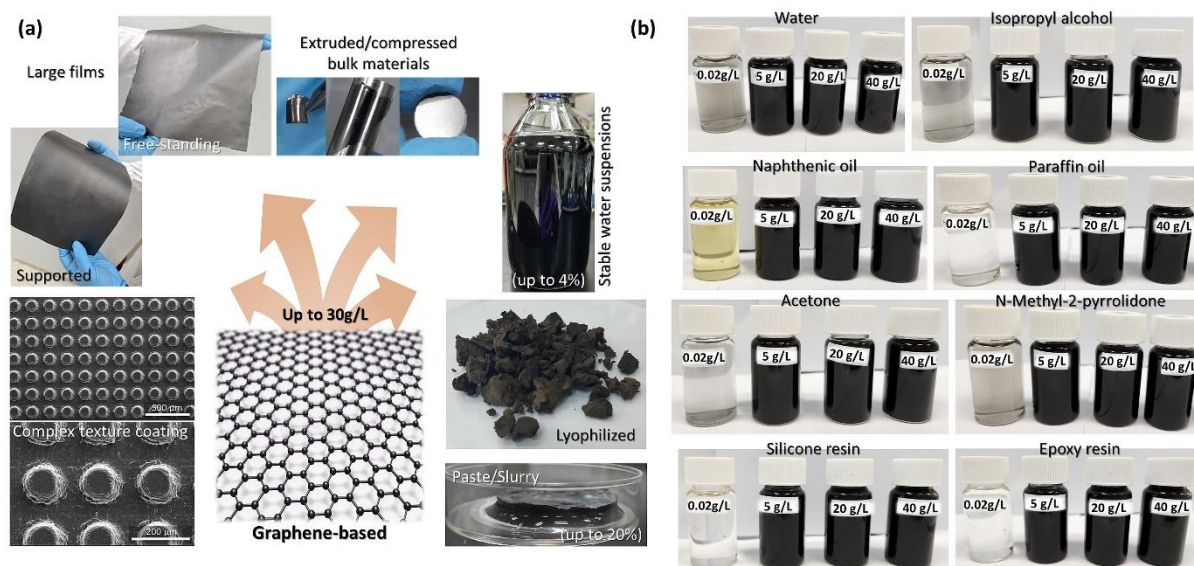


**Figure S6.** Processability and solvent stability. (a) SEM and photographic images of the products yielded by the  $G_{eh}$  platform, allow the adaptation of the outcome depending on the target applications. Examples include coatings of texturized/patterned complex surfaces, large (A4 size) films supported on Cu foil or free-standing, extruded bulk materials and pastilles, highly concentrated water suspension, lyophilized powder, and highly concentrated paste/slurry. (b) Photographic images of  $G_{eh(6)}$  dispersions, with more than 3 orders of concentration range, after 30 min of sonication and 30 min resting in a series of solvents, oils, and resins of industrial interest.

Moreover, due to its amphiphilicity, besides its water stability,  $G_{eh}$  also forms stable dispersions in most hydrophilic and hydrophobic solvents, oils, and resins commonly used in industrial formulations (Figure S6b). We observed that there is no concentration limit to its stability in the different media, and, in fact, stability is mostly favored in higher concentrations until reaching a gel point. This behavior associated to  $G_{eh}$ 's amphiphilicity and edge-to-edge assembly suggests soft glassy dynamics promoted by self-stabilization, akin to highly amphiphilic clays such as laponite [25].

#### **Section S4. Mechanical properties**

Through-plane nano and Micromechanical properties of films, before and after annealing, are investigated using AFM (Bruker – Icon Peak force), Peak Force™ Quantitative Nanomechanics (QNM) in air mode. The tips used are RTESPA-300 and RTESPA-525 models, with spring constant  $k = 40N/m$  and  $k = 200N/m$ , respectively. The estimated tip radii are between 8-12 nm in both cases and the

maps are acquired with high resolution (512 samples/line, and 512 lines per image). After collecting maps, the images from different channels are analyzed using the software NanoScope Analysis.

The mechanical maps of samples before and after annealing, presented in Figure S7, are obtained using the same tip, RTESPA 300 ( $k = 40 \text{ N/m}$ ), for better comparison between them. However, the films are also imaged using RTESPA 525 ( $k = 200 \text{ N/m}$ ) for a more accurate determination of the average modulus for the annealed sample, which presents a much higher elastic modulus (Figure S7).

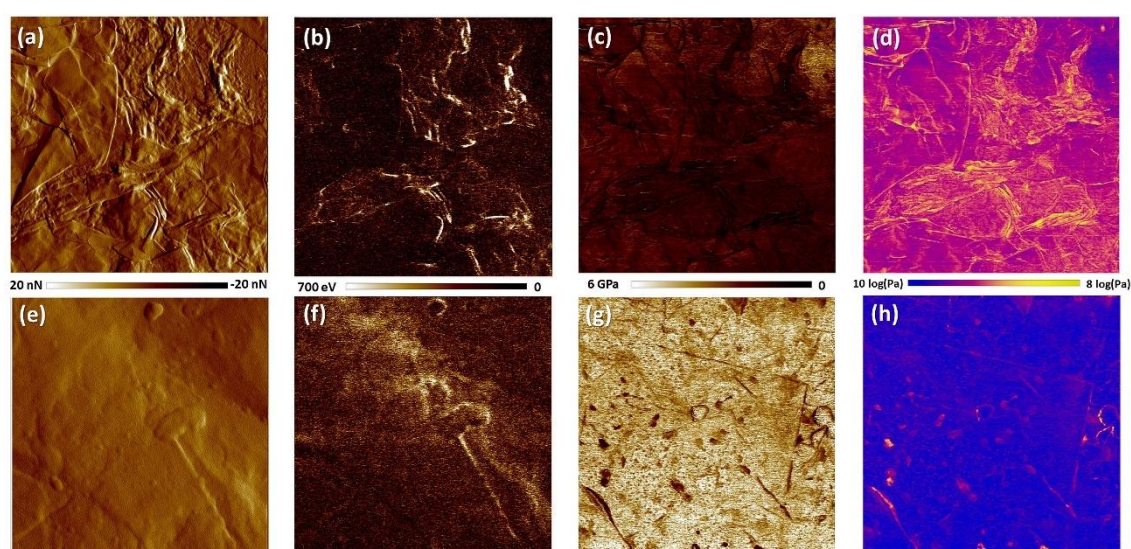


**Figure S7.** AFM micromechanical maps obtained by PF-QNM™, using an RTESPA 300 ( $k = 40 \text{ N/m}$ ) tip; including (a and e) peak force error, (b and f) dissipation, (c and g) stiffness, and (d and h) logarithmic Young's modulus maps of  $G^0_{(6)}$  films before (top row) and after annealing (bottom row), respectively. The maps before and after annealing are normalized, following the same scale for better visualization.

Before annealing, the films present interacting-sheets structures, where fluctuation in mechanical properties close to the edge contacts allows for clear visualization of a reduced stiffness (Figure S7a-d), which is also visible in the peak force error map only before annealing (Figure S7a vs. e). The same fluctuations cause mechanical energy loss and are clearly detected by the dissipation maps (Figure S7b vs. f). At these regions, the overall lower stiffness and defined dips of micromechanical Young's modulus ( $E'_m$ ) reveal the edge lines and corrugations (SI, Figure S7b-d).

After annealing, a smoother film surface is observed, with virtually undetectable sheet edge junctions or corrugations (SI, Figure S7e and f). For better visualization of the elastic modulus, we present both linear and log maps, allowing to observe the disappearance of the moduli dips, a dramatic modulus increase above the scale limit (Figure S7c vs. g), and modulus homogenization after annealing (Figure S7d vs. h).

DMA micromechanical analyses (tensile mode) of the films confirm the mechanical reinforcement after annealing. The storage (elastic) modulus increases two-fold with annealing (from ~10 GPa to ~21 GPa), while the loss (viscous) modulus changes only slightly (from 600 MPa to 800 MPa). This indicates that the films are highly elastic, have a low degree of energy dissipation and low internal friction during deformation. The coefficient of thermal expansion (CTE) of the films also falls two-fold after annealing, demonstrating a strong fixation of the structure. The association of these mechanical behaviors, including the micromechanical ones (Figure S7), resembles that of densely crosslinked polymer networks<sup>[26]</sup>, where the structure becomes fully percolated after crosslinking.

### ***Section S5. Thermal transport***

Thermal images of  $G^0$  films were captured using a Tix500 thermal camera (Fluke, Everett, WA, USA), and treated using SmartView Classic 4.4 software with the reference emissivity set as 0.8 (in the range of purified carbon materials), the relative humidity set to 50% and the environment temperature was set to 21°C (pre-set conditions in the laboratory).

Thermal images of rectangular strips were measured using a hot plate as the heat source, with the temperature set to ~150 °C. Due to its low infrared emissivity (~ 0.03), a polished Cu film was used to cover the heat source for preventing the transmission of background infrared emission. Specimens measuring 10x80mm were prepared and placed directly onto the heated Cu sheet, and thermal images were captured upon thermal stabilization (~20 min). The  $G^0_{(6a)}$  film strip (after annealing) was compared to two commercial carbon/graphene-based thermal conductive films, graphene-based

( $T_{G(\text{film})}$ ) and graphite-based ( $T_{Gr(\text{film})}$ ), and a non-conductive paper strip ( $\alpha \sim 0.07 \text{ mm}^2/\text{s}$ ). The setup for the thermal imaging is demonstrated in Figure S8a.

Thermal imaging measurements were also performed on a 5-inch solvent casted film (Figure S8b), before ( $G^0_{(6)}$ ) and after annealing ( $G^0_{(6a)}$ ), using a heat source with the temperature set to 200 °C. Thermocouples were set 1 inch apart from the heat source, to compare the conducted heat with the radiation heat captured by the thermal camera (Figure S8c). The film emissivity at thermodynamic equilibrium was obtained using the Stefan–Boltzmann law,  $P = \epsilon\sigma T^4$ , where  $\epsilon$  is the film emissivity,  $\sigma$  is the Stefan–Boltzmann constant, and  $T$  is the surface temperature. The integrated emissivity  $\epsilon$  of the surface is  $\epsilon = \epsilon_i(T_i/T)^4$ , where  $\epsilon_i$  is the emissivity used for thermal imaging (0.8),  $T_i$  is the infrared temperature (25°C), and  $T$  is the temperature measured with the thermocouple (56°C), resulting in  $\epsilon = 0.03$  for  $G^0_{(6a)}$ . The  $\epsilon$  was also measured for  $G^0_{(6)}$ ,  $\epsilon \sim 0.1$ , however, this value is not trustworthy since annealing takes place during the measurement and both radiation and conduction heat-related temperatures are unstable.

Laser flash analysis (LFA) was used to characterize the anisotropic thermal diffusivity of the films, as it is commonly used to measure high thermal conductive thin film materials. Free standing samples were pre-cut into a circular shape with diameter  $\sim 24.6 \text{ mm}$  before loading into the standard through-plane and customized in-plane sample holders for Netzsch LFA 467. The measurements were performed with the Netzsch LFA 467 system using a standard model, which is a modified version of Cape & Lehman model considering both radial and axial heat losses. In addition, the in-plane model for the calculation of diffusivities takes into consideration our sample's anisotropic nature. Whereby, the back surface of the sample is heated by a xenon (higher power) with pre-defined pulse width (Figure S8d). The temperature rise signal  $T_{(t)}$  is monitored on the top surface with the help of an IR detector (typically InSb or MCT). The thermal diffusivity of the sample is given by:

$$\lambda = 0.1388 \frac{d^2}{t_{1/2}}$$

Whereby  $d$  is the thickness of the thin film sample and  $t_{1/2}$  is the half-time it takes for the temperature to rise to the maximum temperature. This simplified model assumes an isotropic and adiabatic system.

The specific heat capacity ( $C_p$ ) of our films was also measured using the laser flash comparison method, by contrasting it with a reference material that possesses a known specific heat capacity<sup>[27]</sup>. To achieve accurate results, the reference sample must have a comparable cross-sectional shape, thermal conductivity values, and be suitable for the temperature range being studied (e.g. graphite). Here, we measured the value of  $C_p$  for our films starting from room temperature up to 300 °C. As plotted in Figure S8e, the value increases almost linearly from 1.8 to 2.3, with increasing temperature. These  $C_p$  values were used to calculate the thermal conductivity presented in Figure S8d.

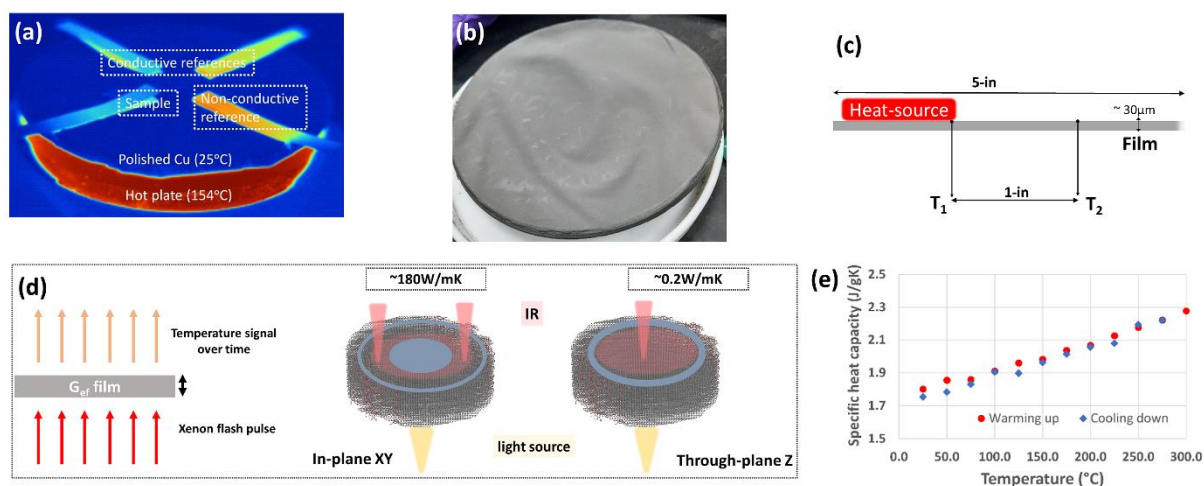


**Figure S8.** Thermal transport characterizations. (a) Thermal image showing the setup used to obtain Figure 6d. (b) Photographic image of the film with 5 inches in diameter and 100  $\mu\text{m}$  thickness used to obtain the thermal image in Figure 6e. (c) Schematic drawing showing the setup to measure the conductive heat values used to calculate  $\epsilon$ , where a heat source  $T_1$  is heated to 200 °C and temperature readings are made in  $T_2$ . (d) Schematic drawing showing the light flash technique used for measuring the thermal diffusivity of the films. Free-standing samples with thickness varying between 50-400  $\mu\text{m}$  were pre-cut to a circular shape with a diameter of 1 inch, to be fitted into the pre-defined sample holders. (e) Specific heat capacity ( $C_p$ ) measurement of  $G^0_{(6a)}$ , used for determining the thermal conductivity of the films.

### Section S6. Electrical transport

Sheet resistance ( $R_s$ ) is a common electrical property used for the characterization of conducting and semiconducting uniform thin films. The main advantage of this parameter is that it is independent of the sample size and it can be measured directly via a 4-point probe method.

$$R_s = \frac{\rho}{t}$$

It is defined as the resistivity ( $\rho$ ) of a material divided by its thickness ( $t$ ), with ohms ( $\Omega/\text{sq}$ ) units.

The most common method for measuring in-plane sheet resistance is by employing the 4-point probes setup to eliminate the contact resistance (Figure S9a). A direct current is applied between the outer two probes and a voltage drop is measured between the inner two probes. The sheet resistance can then be calculated using the following equation:

$$R_s = \frac{\pi}{\ln(2)} \frac{\Delta V}{I}$$

This equation is valid only if the thickness of the material being tested is less than 40% of the spacing between the probes ( $d = 1 \text{ mm}$ ) and the lateral size of the sample is sufficiently larger. Otherwise, other geometric correction factors are required to account for the size, shape and thickness of the sample – which are included in the dasoleng measurement setup. Thus, the same batch of samples used for thermal diffusivity measurements, without further preparation, was used for sheet resistance measurements using a dasoleng 4-probe measurement setup.

For the through-plane measurements, a 4-point probe device is also used to measure the electrical conductivity of the film to eliminate contact resistance. However, a device was fabricated on a 4-inch  $\text{SiO}_2$  (285 Å)/Si wafer. First, the bottom layer of metal contacts which consists of Ti (50 Å)/Au (1000 Å) was deposited via electron beam evaporator system (AJA ATC-E) with the aid of a thermal tape mask. Next,  $G_{\text{eh}}$  was drop-casted onto a pre-defined square with an area of 20 mm x 20 mm. The sample was left to dry in fume-hood for few hours. Finally, the top layer of metal contacts which consists of Au (1000 Å) was deposited using the same method as described above. Thus, the device's metal electrodes deposited on the bottom and top sandwich the film (Figure S9b).

A sinusoidal alternating current is applied between a pair of bottom and top contacts and the resultant voltage drop is measured between the remaining pair with a lock-in amplifier (Stanford Research SR830). The resistivity (conductivity) can then be calculated using the following equation:

$$\rho = \frac{\Delta V A}{I t}$$

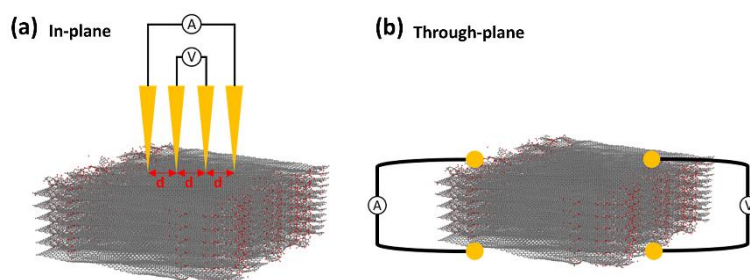


**Figure S9.** Schematic representations showing the four-point probe measurement setups. **(a)** In-plane measurement with four electrical contacts with equal spacing  $d$  in a line, where the current  $I$  is applied on the outer two probes and the resultant voltage  $\Delta V$  drop is measured between the inner two probes. **(b)** Through-plane measurement with two electrical contacts on the top and two on the bottom of the film.

**Table S7.** Sheet resistance and conductivity of the films.

Sample	Thickness ( $\mu\text{m}$ )	Sheet resistance ( $\Omega\text{sq}^{-1}$ )
1	300	0.033
2	300	0.035
3	390	0.051
4	370	0.133
5	380	0.255

### **Section S7. Compositional, morphological and physicochemical characterization methods**

The substrates (Si, Si/SiO<sub>2</sub> or Si/Au) used for the characterization of isolated flakes and flake clusters were washed by immersion in acetone and isopropanol alcohol under sonication (5 min each) and thoroughly dried, then, highly diluted dispersions of G<sub>eh</sub> (< 0.01mg/mL) were drop casted onto them. These substrate-deposited samples were investigated by a series of microscopy and spectroscopy techniques, as described below. The bulk compositional characterizations were performed directly in solvent casted free-standing films (see details below and in Section S2).

**For scanning electron microscopy (SEM)**, samples are drop casted directly onto Si and Au-coated Si substrates and the analyses are carried out in a FEI Verios 460L **field-emission scanning electron microscope (FESEM)** operating at 2 kV. SEM-EDX mappings were performed using a Zeiss Evo 10, operating, operated at 6.3 kV.

For **high-resolution transmission electron microscopy (HRTEM)**, samples were drop casted on Lacey carbon gold TEM grids (TedPella). HRTEM was performed using a FEI Talos F200X combining high-resolution STEM and TEM imaging with **energy dispersive x-ray spectroscopy (EDS)** using four silicon drift detectors (SDDs), and **Selected Area Electron Diffraction (SAED)** for determining the periodicity in the HRTEM images revealing the crystal structure of the materials.

**Optical images** are obtained on Si/SiO<sub>2</sub> substrates using an Olympus optical microscope.

**X-ray photoelectron spectroscopy (XPS)** was performed using Kratos AXIS Supra<sup>+</sup>. Each spectrum is an average of 5 scans with an emission current of 150 eV and a step-size of 1 eV for survey spectra, and emission current of 20 eV, and a step-size of 0.05 eV for high-resolution spectra. An ion gun was used during each scan to neutralize the charging phenomena. Data analysis and fitting were performed with ESCApe software after Shirley background subtraction. The deconvolution of C 1s peak was performed considering an asymmetric nature of aromatic sp<sup>2</sup> components fitted (asymmetry parameter = 0.14). The contributions of all the other functional groups and the sp<sup>3</sup> C 1s signals were fitted using standard symmetric Gaussian and Lorentzian curves.<sup>[28]</sup>

**Secondary Ion Mass Spectrometry (SIMS)** measurements were performed using the CAMECA IMS SC Ultra instrument. Cesium primary beam with high impact energy (16 keV) and density (450 nA for a beam with 50 microns diameter) was used to make a full profile of carbon films. The beam was rastered over 250 x 250 microns, whereas the analysis area was limited to 100 x 100 microns. The angle of the incident was 51° and to avoid the shadowing effect the analysis area was shifted 70 microns along the incident ions. With positive detector polarity, all the signals were registered as Cs<sub>2</sub>X<sup>+</sup> cluster ions and each signal was normalized to the Cs<sub>2</sub><sup>+</sup> signal. Even though carbon and oxygen



sensitivity is not very high (in the range of 0.01%-0.1% for both elements) the mode is known to be semi-quantitative<sup>[29]</sup>. Concentration calibration of the carbon signal was based on the analysis of the pure Highly Ordered Pyrolytic Graphite (HOPG) sample. The average intensity of the  $Cs_2C^+$  and  $Cs_2^+$  signals was 12820 and 985673 counts, respectively and thus the ratio of these two signals was assigned to 100% concentration of carbon. For oxygen concentration calibration, a HOPG sample implanted with oxygen was used. It was determined that the detection limit of oxygen is 0.0097% which corresponds to a single count of the  $Cs_2O^+$  signal. The average intensity of the  $Cs_2^+$  signal was the same in the previous experiment and thus the ratio of these two signals was assigned to 0.0097% concentration of oxygen. Based on the semi-quantitative nature of this measurement mode it was assumed that  $Cs_2X^+/Cs_2^+$  ratios scale linearly with concentrations of carbon and oxygen. The validity of this assumption was verified by monitoring the sum of the determined carbon and oxygen concentrations. It was found to be  $100 \pm 1\%$  for all data points and all samples. Given that the calibration of both signals was performed independently, it could be concluded that the elemental composition of samples was determined with reasonable accuracy.

A simultaneous **TGA/DSC** analyzer **SDT 650** (TA Instruments) calibrated with sapphire and zinc standards is used to study the thermal behavior of the materials. Film pieces ( $\sim 15$  mg) are placed in a ceramic pan (90  $\mu$ l) with the punctured lid and heated at a constant rate (0.5°C/min) under an air atmosphere. An empty ceramic pan is used as a reference. As the temperature changes, the instrument simultaneously measures the sample's weight change and heat flow.

**Atomic force microscopy (AFM)** topography images are acquired in a Bruker Dimension Icon Microscope operated in tapping mode and scan lines of 512 and the height profile images are obtained using the open-source AFM image processing tool Gwyddion.

**Confocal Raman spectroscopy** is carried out in a Witec Alpha 300R, with excitation wavelength of 532 nm and a 100x objective with a numeric aperture of 0.9. The spectra are normalized with respect to the G band intensity.

## Section S8. G<sup>0</sup>'s properties summary

**Table S8.** General properties of G<sup>0</sup><sub>(6a)</sub> films.

Physical	Flexible, bendable film
Color	Metallic, shiny
Typical thickness range ( $\mu\text{m}$ )	4-400
Density ( $\text{kgm}^{-3}$ )	1,100-1,500
<sup>[1]</sup> Electrical conductivity ( $\text{Sm}^{-1}$ ) (In-Plane/Through-Plane)	320,000/3.8
<sup>[2]</sup> Thermal conductivity ( $\text{Wm}^{-1}\text{K}^{-1}$ ) (In-Plane/Through-Plane)	180 / 0.16
<sup>[3]</sup> Anisotropy (Electrical/Thermal)	84,210 / 1125
<sup>[4]</sup> Specific heat capacity ( $\text{Jkg}^{-1}\text{K}^{-1}$ )	1,700-2,000
<sup>[5]</sup> Coefficient of thermal expansion ( $\text{ppmK}^{-1}$ )	$-4 \times 10^{-6}$
<sup>[6]</sup> Young's modulus (Pa)	$2 \times 10^{10}$
<sup>[7]</sup> Stability (K)	up to 1373

[1]: The conductivity values were measured at room temperature, 298 K in a cryostat system with the in-plane and through-plane devices;

[2]: The conductivity values were measured at room temperature, 298 K via the laser flash analysis method;

[3]: The anisotropy values were calculated based on the ratio of the in-plane value over the through-plane value;

[4]: The specific heat capacity value was obtained with the comparison method using a graphite reference sample via the laser flash analysis measurement;

[5]: The coefficient of thermal expansion was measured with an annealed sample using a TMA system;

[6]: The Young's modulus was measured with the tapping mode of an atomic force microscope system;

[7]: Stability tests were conducted on samples by annealing treatment up to 1100 °C.

### Acknowledgement and funding information

This research, including the computational calculations, was carried out at the Centre for Advanced 2D Materials (CA2DM), funded by the National Research Foundation, Prime Minister's Office, Singapore, under its Medium-Sized Centre Programme, and by the Singapore Ministry of Education under its Research Centre of Excellence award to the Institute for Functional Intelligent Materials, National University of Singapore (I-FIM, project No. EDUNC-33-18-279-V12). The National Supercomputing Centre, Singapore (NSCC) is acknowledged for providing computational resources. P.E. and J.T. acknowledge the assistance provided by the Research Infrastructure NanoEnvicZ, supported by the Ministry of Education, Youth and Sports of the Czech Republic under Project No. LM2018124.

## References

- [1] P. Giannozzi, O. Andreussi, T. Brumme, O. Bunau, M. Buongiorno Nardelli, M. Calandra, R. Car, C. Cavazzoni, D. Ceresoli, M. Cococcioni, N. Colonna, I. Carnimeo, A. Dal Corso, S. de Gironcoli, P. Delugas, R. A. DiStasio, A. Ferretti, A. Floris, G. Fratesi, G. Fugallo, R. Gebauer, U. Gerstmann, F. Giustino, T. Gorni, J. Jia, M. Kawamura, H.-Y. Ko, A. Kokalj, E. Küçükbenli, M. Lazzeri, M. Marsili, N. Marzari, F. Mauri, N. L. Nguyen, H.-V. Nguyen, A. Otero-de-la-Roza, L. Paulatto, S. Poncé, D. Rocca, R. Sabatini, B. Santra, M. Schlipf, A. P. Seitsonen, A. Smogunov, I. Timrov, T. Thonhauser, P. Umari, N. Vast, X. Wu, S. Baroni, *J. Phys. Condens. Matter* **2017**, *29*, 465901.
- [2] J. P. Perdew, K. Burke, M. Ernzerhof, *Phys. Rev. Lett.* **1997**, *78*, 1396.
- [3] A. M. Rappe, K. M. Rabe, E. Kaxiras, J. D. Joannopoulos, *Phys. Rev. B* **1990**, *41*, 1227.
- [4] S. Grimme, *J. Comput. Chem.* **2006**, *27*, 1787.
- [5] V. Barone, M. Casarin, D. Forrer, M. Pavone, M. Sambri, A. Vittadini, *J. Comput. Chem.* **2009**, *30*, 934.
- [6] H. J. Monkhorst, J. D. Pack, *Phys. Rev. B* **1976**, *13*, 5188.
- [7] S. Plimpton, *J. Comput. Phys.* **1995**, *117*, 1.
- [8] K. Chenoweth, A. C. T. van Duin, W. A. Goddard, *J. Phys. Chem. A* **2008**, *112*, 1040.
- [9] Jmol: an open-source Java viewer for chemical structures in 3D. <http://www.jmol.org/>
- [10] J. Chen, Y. Zhang, M. Zhang, B. Yao, Y. Li, L. Huang, C. Li, G. Shi, *Chem. Sci.* **2016**, *7*, 1874.
- [11] M. C. F. Costa, V. S. Marangoni, M. Trushin, A. Carvalho, S. X. Lim, H. T. L. Nguyen, P. R. Ng, X. Zhao, R. K. Donato, S. J. Pennycook, C. H. Sow, K. S. Novoselov, A. H. Castro Neto, *Adv. Mater.* **2021**, *33*, 2100442.
- [12] V. S. Marangoni, M. C. F. Costa, P. R. Ng, H. T. L. Nguyen, M. Trushin, A. Carvalho, X. Zhao, S. J. Pennycook, R. K. Donato, A. H. Castro Neto, *Mater. Today Chem.* **2021**, *21*, 100542.
- [13] G. Quek, Y. Su, R. K. Donato, R. J. Vázquez, V. S. Marangoni, P. R. Ng, M. C. F. Costa, B. Kundukad, K. S. Novoselov, A. H. C. Neto, G. C. Bazan, *Adv. Electron. Mater.* **2022**, *8*, 2100942.
- [14] H. L. Tan, P. R. Ng, M. Trushin, G. K. W. Koon, K. Z. Donato, M. C. F. Costa, R. K. Donato, A. H. Castro Neto, *Mater. Today Chem.* **2023**, *27*, 101296.
- [15] M. C. F. Costa, P. R. Ng, S. Grebenchuck, J. Y. Tan, G. K. W. Koon, H. L. Tan, C. R. Woods, R. K. Donato, K. S. Novoselov, A. H. Castro Neto, *Carbon N. Y.* **2023**, *208*, 140.
- [16] F. Farivar, P. L. Yap, K. Hassan, T. T. Tung, D. N. H. Tran, A. J. Pollard, D. Losic, *Carbon N. Y.* **2021**, *179*, 505.
- [17] Z. Q. Li, C. J. Lu, Z. P. Xia, Y. Zhou, Z. Luo, *Carbon N. Y.* **2007**, *45*, 1686.
- [18] F. L. Thiemann, P. Rowe, A. Zen, E. A. Müller, A. Michaelides, *Nano Lett.* **2021**, *21*, 8143.
- [19] R. Ruoff, *Nat. Nanotechnol.* **2008**, *3*, 10.
- [20] A. L. Moore, L. Shi, *Mater. Today* **2014**, *17*, 163.
- [21] S. Paredes, Y. Madhour, G. Schlottig, C. L. Ong, T. Brunswiler, *ECS Trans.* **2014**, *64*, 253.
- [22] S. Eigler, C. Dotzer, A. Hirsch, M. Enzelberger, P. Müller, *Chem. Mater.* **2012**, *24*, 1276.
- [23] In *IUPAC Compend. Chem. Terminol.*, International Union Of Pure And Applied Chemistry (IUPAC), Research Triangle Park, NC, **2014**.

- [24] W. Zhao, S. L. Hsu, S. Ravichandran, A. M. Bonner, *Macromolecules* **2019**, *52*, 3367.
- [25] K. Suman, Y. M. Joshi, *Langmuir* **2018**, *34*, 13079.
- [26] D. Guseva, V. Rudyak, P. Komarov, B. Bulgakov, A. Babkin, A. Chertovich, *Polymers (Basel)*. **2018**, *10*, 792.
- [27] K. Shinzato, T. Baba, *J. Therm. Anal. Calorim.* **2001**, *64*, 413.
- [28] A. Kovtun, D. Jones, S. Dell'Elce, E. Treossi, A. Liscio, V. Palermo, *Carbon N. Y.* **2019**, *143*, 268.
- [29] W. J. Oh, J. S. Jang, Y. S. Lee, A. Kim, K. J. Kim, *Appl. Surf. Sci.* **2018**, *432*, 72.